Research Article

Nano Research
2019, 12(11): 2760–2765

ISSN 1998-0124 CN 11-5974/O4
https://doi.org/10.1007/s12274-019-2510-9

Special interstitial route can transport nanoparticles to the brain bypassing the blood-brain barrier

Nan Hu[1,2,3,§], Xiaoli Shi[1,2,§] (✉), Qiang Zhang[1,2], Wentao Liu[1,2], Yuting Zhu[1,2], Yuqing Wang[1,2], Yi Hou[4], Yinglu Ji[1], Yupeng Cao[1,2], Qian Zeng[1,2], Zhuo Ao[1,2], Quanmei Sun[1,2], Xiaohan Zhou[1,2], Xiaochun Wu[1], and Dong Han[1,2] (✉)

[1] *CAS Center for Excellence in Nanoscience, National Center for Nanoscience and Technology, Beijing 100190, China*
[2] *School of Future Technology, University of Chinese Academy of Sciences, Beijing 100049, China*
[3] *Department of Traditional Chinese Medicine, Chengde Medical University, Chengde 066000, China*
[4] *Institute of Chemistry, Chinese Academy of Sciences, Beijing 100190, China*
[§] *Nan Hu and Xiaoli Shi contributed equally to this work.*

Received: 10 July 2019 / **Revised:** 24 August 2019 / **Accepted:** 27 August 2019

ABSTRACT

Nowadays, nanoparticles (NPs) are considered to be ideal tools for bioimaging and drug delivery. Although increasing research has focused on NP biodistribution, transportation in the interstitial architecture has been neglected. The entire body is connected by the interstitial architecture, which can provide a long-range and direct pathway for NP biodistribution in a nonvascular system. In this study, we report that 10-nm gold NPs injected directly into the interstitial architecture of the tarsal tunnel of rats (intervaginal space injection (ISI)) were delivered to the brain without crossing the blood-brain barrier. Furthermore, $NaGdF_4$ nanoparticles were used to explore the transportation route by magnetic resonance imaging. The results demonstrated that, after ISI, the $NaGdF_4$ nanoparticles were transported through the perivascular interstitial space of the carotid arteries and brain vessels to the brain. This is a special nonvascular transportation route like a stream based on the interstitial architecture that provides an alternative pathway for NP biodistribution.

KEYWORDS

nanoparticles, interstitial stream, mass transportation, blood-brain barrier, magnetic resonance imaging

1 Introduction

With the development of nanotechnology, nanoparticles (NPs) have received tremendous attention in bioimaging, therapy, and drug delivery fields [1–4]. The advantages of NPs such as their easily modified platforms, large surface-to-volume ratios, and controlled sizes and shapes facilitate their overcoming of various biological barriers. However, these advantages should be considered as a double-edged sword, as NPs can also induce severe side effects [5]. Therefore, it is imperative to fully understand the biodistribution and transportation of NPs after administration. Taking gold NPs (AuNPs) as an example, there have been a number of studies on their biodistribution and pharmacokinetics [5–8]. Most work has emphasized the circulation of AuNPs in the blood stream to tissues and organs through the vascular system, but nonvascular system transportation by interstitial architecture has rarely been investigated. Furthermore, although the nonvascular pathways for the passage of fluid into and out of the brain have been a hotpoint, the pathways are local transportation observed by injecting the marker into ventricular invasively [9–11]. As a whole body exited structure, we wonder if there is a long-range transportation route within the interstitial architecture.

The interstitial architecture is a hierarchical network located between cells, parenchymal functional tissues, and organs throughout the body. On a nanometre scale, the network is composed of fibres arranged to form a densely connected tissue. On the macroscopic scale, the interstitial architecture (fascia) wraps around blood vessels and forms the perivascular interstitial space [12, 13]. With its structural features, the interstitial architecture may perform connection, filling, fixation and nutritional functions. Similar to the well-organized flow of blood stream in the vascular system, there is a long-rang and high-efficiency connecting route within the interstitial architecture. We also use "interstitial stream" to describe the orientable interconnecting behavior. The interstitial stream, a typical flattened connection route, rather than the fractal structure of blood stream, leads to direct mass transmission of flow, information and stress force in nonvascular system. Thus, the biodistribution of NPs by the interstitial architecture should be considered as important as that by the vascular system and must be taken into serious consideration.

Here, we report the delivery of 10 nm AuNPs by interstitial architecture to the brain after direct injection into the tarsal tunnel interstitial architecture of rats, denoted as intervaginal space injection (ISI). This delivery to the brain bypasses the blood-brain barrier (BBB). With $NaGdF_4$ NPs as agents, the magnetic resonance imaging (MRI) results demonstrated that the transportation to the brain was based on the interstitial architecture and occurred through the perivascular interstitial space of carotid arteries and brain vessels.

2 Experimental

2.1 Preparation and characterization of AuNPs

AuNPs were prepared by a well-known procedure [14]. Briefly, we used $NaBH_4$ to reduce $HAuCl_4$ and obtain Au nanocrystallites, which were then placed in a solution of CTAB (0.1 M, 500 mL), $HAuCl_4$

Address correspondence to Dong Han, dhan@nanoctr.cn; Xiaoli Shi, shixl@nanoctr.cn

(23.8 mM, 5.25 mL), and ascorbic acid (0.1 M, 75 mL) to grow. The obtained AuNPs were dispersed in deionized water, then dripped the suspension in a copper grid and dried. The AuNPs were observed by TEM (Ht-7700, Hitachi) for size and shape analysis.

2.2 Preparation and characterization of $NaGdF_4$ NPs

Typically, $GdCl_3{\cdot}6H_2O$ (0.371 g, 1 mmol) was dissolved in a mixed solution of oleic acid (OA, 14 mL) and octadecene (16 mL). Under nitrogen, the mixture was heated to 150 °C to homogenize, then 10 mL of a methanol solution containing NaOH (0.100 g, 2.5 mmol) and NH_4F (0.148 g, 4 mmol) was added once the mixture had cooled to room temperature. After that, the obtained mixture was stirred at 50 °C for 30 min, followed by vacuum removal of methanol for 10 min at 100 °C. The solution was then heated to 300 °C under atmospheric pressure by electromantle and maintained for 1 h at 300 °C for 1 h under nitrogen protection. The preparation was terminated by cooling the reaction mixture down to room temperature. The resultant nanoparticles, that is, $NaGdF_4$, were precipitated by ethanol, collected by centrifugation, washed with ethanol several times, and finally redispersed in tetrahydrofuran (THF) or cyclohexane for further experiments. For the next experiment for the ligand exchange, 100 mg of PEG-phosphate ligand was mixed with ca. 10 mg OA-coated $NaGdF_4$ nanoparticles in 10 mL of THF. Then, the mixed solution was stirred at room temperature overnight. PEG-coated $NaGdF_4$ particles were acquired after precipitation by cyclohexane, washing with cyclohexane three times, and drying under vacuum at room temperature. The obtained NPs were then dissolved in saline for use.

2.3 Fluorescence imaging of the interstitial stream

A Sprague Dawley (SD) rat purchased from Beijing Vital River Experimental Animal Corporation (Beijing, China) was anesthetized with 3.5% chloral hydrate (mL·kg^{-1} body) intraperitoneally. The skin of the leg was cut to expose the great saphenous vein (GSV), and 100 μL of clinical fluorescein sodium (2% physiological saline solution w/v) was injected into the tarsal tunnel on the left ankle bone, where the nerve and vessels were sheathed by the interstitial architecture space and connected to the remote interstitial architecture (Fig. 1(e)). Imaging was performed before and after injection with a fluorescence stereomicroscope (Carl Zeiss).

2.4 AuNP delivery to the brain of normal rats and content analysis

Male SD rats (6 weeks old) were divided into ISI and intravenous injection (IVI) groups, with each group having 7 subjects. The rats were weighed and anesthetized. In the IVI group, a 500 μL AuNP suspension was injected into the GSV using 1 mL syringes. In the ISI group, the injection point was selected as the interstitial structure of the tarsal tunnel (Fig. 1(e)). One hour after injection, the rats were euthanized by an overdose of 3.5% chloral, and heart perfusion was performed with Ringer's fluid to exclude the blood in the cerebral vessels. The brain from each subject was then excised and washed thoroughly with phosphate-buffered saline (PBS), followed by removal of residual water from the surface with filter paper and weighing. Each sample was placed in a separate beaker and digested with aqua regia (3 mL) [9]. A standard curve was obtained using Au standard solutions diluted in a solution containing 2% HNO_3 and 1% HCl (0.2, 0.5, 1, 2, and 5 ppb) for inductively coupled plasma mass spectrometry (ICP-MS) measurements. (Perkinelmer NexION 300X)

2.5 Statistical analysis

The relative Au content obtained by ICP-MS was calculated using Eq. (1)

$$C = N_{con}/N_{brain} \quad (1)$$

where N_{con} is the Au content in the brain and N_{brain} is the weight of the brain. Results are given as mean ± standard deviation (S.D.). The ISI:IVI Au content ratios were calculated by dividing the Au content from the brain and blood after ISI by the content from the brain and blood after IVI, and the averages were calculated. Student's *t*-tests were used to compare differences between the two groups, with $p < 0.05$ being considered statistically significant.

2.6 Bilateral common carotid artery occlusion (BCCAO) experiment

Anesthetized rats were fixed in a supine position, hair was removed in the anterior cervical region, and the area was disinfected with iodine solution. The skin was cut through the midline of the neck, and the sternocleidomastoid was bluntly separated to explore both sides of the common carotid artery. Then, surgical sutures were used to tie the bilateral common carotid arteries tightly for 20 min before injection (Fig. S1(a) in the Electronic Supplementary Material (ESM)).

2.7 Sample preparation and TEM imaging

The rat was sacrificed by overdose of 3.5% chloral hydrate intraperitoneally. Then, the brain was separated from the body, cut into 1 mm^3 and washed with PBS. 2.5% (v/v) glutaraldehyde was used to fix the sample overnight, and then 1% phosphate-buffered OsO_4 was used to fix the samples for 3 h. After that the samples were dehydrated by a graded series of 30%, 50%, 70%, 85%, 95%, and 100% for 7 min each. The dehydrated samples were then washed with acetone three times, and after embedded with resin overnight, and they were polymerized in an incubator under a graded series conditions of 37 °C for 12 h, 45 °C for 12 h, and 60 °C for 48 h. The prepared samples were sliced into 60 nm thick using an ultramicrotome (Leica EM UC7), and stained with uranyl acetate and lead citrate. Ultrastructure images of the brain were obtained using a transmission electron microscope (TEM, Hitachi, H-7500)

2.8 MRI scans

In vivo MRI acquisitions were performed using a 7.0 T MRI scanner (Bruker Biospin, Billerica, MA, USA) with a rat head coil. In normal conditions, rats were divided into IVI and ISI groups. After anesthetization, rats were placed into an MRI scanning cradle in a prone position. Two-dimensional T1-weighted rapid acquisition with relaxation enhancement (RARE) pulse sequences were used to display

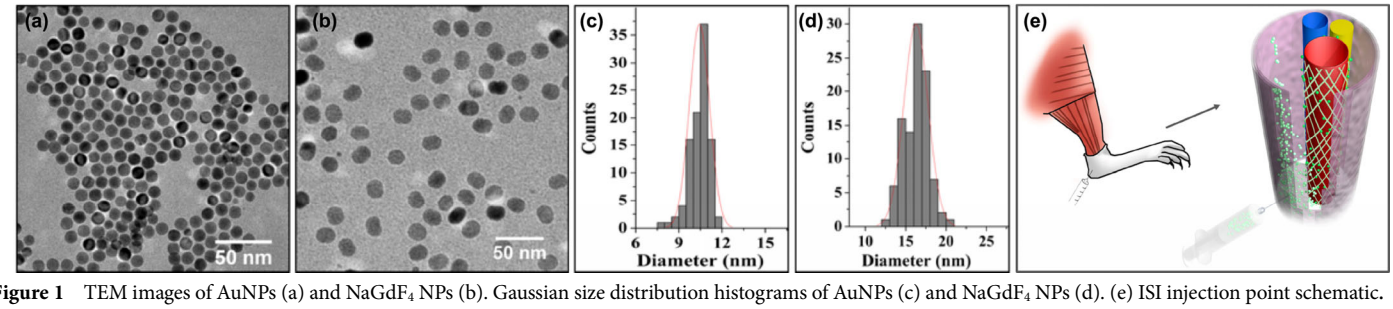

Figure 1 TEM images of AuNPs (a) and $NaGdF_4$ NPs (b). Gaussian size distribution histograms of AuNPs (c) and $NaGdF_4$ NPs (d). (e) ISI injection point schematic.

the signal enhancement of paramagnetic NPs. The T1-RARE imaging parameters were repetition time (TR) = 595 ms, effective echo time (TE) = 5.48 ms, RARE factor = 2, field of view (FOV) = 3.5 cm × 3.5 cm, matrix size = 256 × 256, slice thickness = 10 mm, and number of averages = 3. Before injecting, T1-RARE scanning was performed and then 0.5 mL $NaGdF_4$ NP suspension was injected into the selected point, and T1-RARE scanning was performed again 30 min after administration. After T1-RARE pulse sequence acquisitions, we also used three-dimensional (3D) DCE-MRA to display the vascular structure. The DCE-MRA imaging parameters were TR = 1.65 ms, TE = 12.3 ms, FOV = 2.8 cm × 2.8 cm, matrix size = 256 × 256, slice thickness = 0.3 mm, and number of averages = 1.

In the pathological conditions, BCCAO and MRI scans were performed as described above. All animal experiments in this study were approved by the Committee at the Institute of the Chinese Academy of Medical Science.

3 Results and discussion

3.1 Characterization of AuNPs and $NaGdF_4$ NPs

The sizes and shapes of the AuNPs and $NaGdF_4$ NPs were observed by TEM. As shown in Figs. 1(a) and 1(c), the AuNPs had a spherical morphology with an average diameter of 10.43 ± 0.70 nm taken from 100 NPs. Figures 1(b) and 1(d) are TEM images of the $NaGdF_4$ NPs, which also had a spherical morphology and an average diameter of 16.27 ± 1.50 nm taken from 100 NPs.

3.2 Au content in the brain of normal rats

In a previous study, we quantitatively analysed the Au content from AuNPs in the blood and several organs of rats at different time points after IVI and ISI using ICP-MS [14]. The results showed completely different biodistributions of AuNPs in these organs depending on injection methods. The Au content in the blood, liver, spleen, and kidney after ISI was much lower than that after IVI; in the lungs, heart, and intestines, the content was similar; and a higher content was detected in the skin and muscle in the ISI group.

In this study, we first injected 2% fluorescein sodium by ISI. As shown in Movie ESM1, the movement of the interstitial stream in the interstitial architecture is clearly observable. Then, we used the same method as in the previous study to analyse the Au content in the brain at designated time points both by IVI and ISI. As shown in Fig. 2(a), in the IVI group, the Au content in the brain at 5 min was 1.76 ± 1.39 ng·g^{-1} and then decreased to 0.37 ± 0.32 ng·g^{-1} 30 min later, after which the content did not change significantly and was 0.30 ± 0.16 ng·g^{-1} after 24 h. In the ISI group, although the content was lower than that in the IVI group at 5 min, it increased and reached a maximum of 0.67 ± 0.30 ng·g^{-1} at 1 h, which was higher than that in IVI group, then decreased to 0.08 ± 0.06 ng·g^{-1} at 24 h. The ISI:IVI Au content ratios in the brain and blood were used to analyse whether the detected content in the brain originated from blood circulation after ISI. In the brain, the ratios were 0.099, 0.256, 0.762, 1.555, and 0.880 at 5 min, 15 min, 30 min, 1 h, and 4 h after injection, respectively. These values are one order of magnitude higher than those in the blood at the same respective time points (0.004, 0.021, 0.066, 0.055, and 0.084). At 12 and 24 h, the ratios in the brain and blood were similar (Fig. 2(b)), which indicated that the Au in the brain in the ISI group was not from only the blood stream.

Based on these results, we chose 1 h after injection as the time point to further compare the distribution of AuNPs in the brain after ISI and IVI and to explore the delivery of AuNPs by the interstitial architecture. One hour after injection, the Au content in the ISI group (0.92 ± 0.86 ng·g^{-1}) was higher than that in the IVI group (0.52 ± 0.54 ng·g^{-1}), but there was no statistically significant difference between them ($p > 0.05$). In previous studies, it was demonstrated that AuNPs with smaller diameter (2, 10, 15 nm) can cross the BBB and travel to the brain after IVI [7, 15], which agrees with our findings in the IVI group. In the ISI group, our results showed that, at each time point from 5 min to 4 h after injection, the Au content in the blood was clearly lower than that in the IVI group. Thus, the Au content detected in the ISI group was transported not by blood circulation but by other pathways that are not only fast and direct but can also deliver the AuNPs to the brain.

3.3 Au content in the brain after BCCAO

In pathology, BCCAO is used to cause ischemia. It has been reported that, early after the onset of ischemia, the activated matrix metalloproteinases degrade the tight junctions of endothelial cells and thereby open the BBB, which leads to vasogenic edema [16]. In our experiment, the edema phenomenon was detected by TEM in both the IVI and ISI groups after BCCAO (Fig. S1 in the ESM), but the content of AuNPs in the ISI group (0.61 ± 0.34 ng·g^{-1}) was much lower than that in the IVI group (1.54 ± 1.30 ng·g^{-1}). As the BBB integrity degraded after BCCAO, which could significantly increase the blood permeability to the brain, we compared the same injection routes pathologically and physiologically. Regardless of edema status, the distribution of AuNPs in the brain was not significantly different in the ISI group ($p > 0.05$), but it increased significantly after BCCAO (1.54 ± 1.30 ng·g^{-1}) compared with the normal group for IVI (0.52 ± 0.54 ng·g^{-1}) ($p < 0.05$) (Fig. 2(c)).

We deduced that, in the IVI group, the injected AuNPs were delivered to the related tissues and organs via the blood stream, and in the brain vessels, the AuNPs had to cross the BBB to reach the brain parenchyma. When the BBB was destroyed after BCCAO, the AuNPs could flow in much more freely. In the ISI group, on the other hand, although the BBB was disrupted, the delivery of AuNPs was not affected because transportation did not depend on the circulation system and there was no BBB limitation. With the results obtained from the normal and pathological groups, we concluded that, after ISI, the AuNPs injected directly into the interstitial

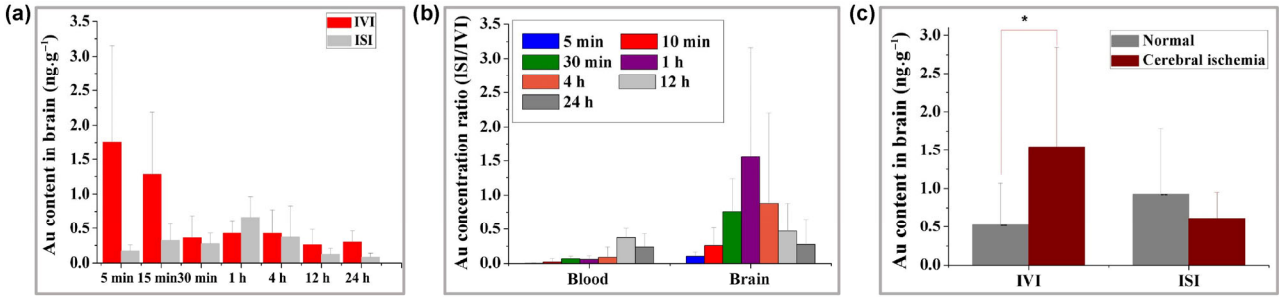

Figure 2 (a) Relative distribution proportions of AuNPs in the brains of normal SD rats at respective time points after IVI (red) and ISI (gray). (b) ISI:IVI AuNP concentration ratios in the brains of normal SD rats at selected time points after injection. (c) Relative distribution proportions of AuNPs in the brains of SD rats 1 h after each injection route in the normal group (dark gray) and BCCAO group (dull red). Data are represented as means ± S.D.

architecture could be transported from the injection point and bypass the BBB to be delivered to the brain by a special route that was not via blood circulation.

Additionally, in our previous studies, we used various tracers to study the fluid behaviour of the interstitium. When we injected fluorescent tracers into the lower leg of human patients, the injected tracer in the lateral ankle dermis was found in two places: loose connective tissue under the dermis and connective tissue surrounding the vessels [17]. We also have used liquid metal as a tracer to research the perivascular interstitial architecture-based pathway. After injecting liquid metal into the wrist intervaginal space of rats, the liquid metal was transported by the interstitial architecture composing the space surrounding vessels and nerves in a nonvascular, longitudinal pathway from fingertips to armpit. In the ultrastructure, the liquid metal was wrapped around the tiny fibrous network of the interstitial architecture [18]. These observations revealed that the structural basis of the interstitial architecture was a fibrous network filled with colloidal fluid. This architecture was simplified as a hierarchical multiphase porous medium (a micrometre-scale hydrophobic fibre network filled with a nanometre-scale hydrophilic porous medium) *in situ* to mimic transportation in the interstitial architecture, which confirmed the transport mechanism as a nano-confined air/water/solid interface around micrometre-scale hydrophobic fibres [19]. An *ex vivo* study of vascular adventitia indicated glycosaminoglycan macromolecules on the surfaces of collagen bundles as a type of hierarchical porous medium that forms superficial macromolecule brushes for the transportation of the interstitial stream [20].

Aside from our studies, there has been other work on nonvascular, interstitial architecture-based transportation. Iliff et al., by infusing fluorescent tracers into the lateral ventricles of mice, observed that traces within the cerebrospinal fluid (CSF) entered the parenchyma through paravascular spaces surrounding the penetrating arteries, and after exchanging with the brain interstitial fluid (ISF) inside the space, the CSF drained along paravenous pathways [9]. It was also found that cerebral vascular basement membranes provide perivascular drainage pathways for the CSF, ISF and soluble compounds to pass into and out of the brain, which has significant implications for neuroimmunology, Alzheimer's disease, and drug delivery to the brain [10]. Most of these studies have focused on the glymphatic role of paravascular spaces for stream in the brain after intracerebral injection, but whole-body transportation by interstitial architecture has been neglected.

3.4 MRI results from normal rats

Next, we aimed to determine the existing pathway of this remarkable transportation from the leg to the brain using MRI. Based on earlier results [18], after ISI, tracers could transport in the interstitial space and surrounded the nerves and vessels. In the anatomical structure, carotid arteries and vertebral arteries are the key junctions to link the body with the brain, where the internal carotid arteries constitute the anterior cerebral circulation and the vertebral arteries supply posterior cerebral circulation. Therefore, we focused on the MR signal changes of the carotid arteries and surroundings before and after injecting $NaGdF_4$ NPs as an MR agent by IVI or ISI. At 0 and 30 min, 2D T1-RARE pulse sequences were acquired. Due to the flow void effect, signals from the blood were not detected and increased signals belonged solely to the agent. As shown in Figs. S2(a) and S2(b) in the ESM, the signals did not increase after IVI in the lumens of the carotid arteries and surroundings. However, after ISI, signals were detected around the vessel lumens of the carotid artery branches (Figs. S2(c) and S2(d) in the ESM). The agent was not transported in the vessels but instead in the surrounding interstitial architectural after ISI.

Subsequently, 3D dynamic contrast-enhanced MR angiography (DCE-MRA) was performed. Figures 3(a)–3(c) show transverse sections from the IVI group; the highlighted signals were clearly circle-shaped in the lumens of common carotid arteries (Figs. 3(a) and 3(e)), carotid artery branches (Figs. 3(b) and 3(f)), and intracranial vessels (Figs. 3(c) and 3(g)), indicating the blood stream and the contained MRI agent. Compared with the IVI group, signals occurred not only in the lumens but also surrounding the lumens with ambiguous shapes in the ISI group (Figs. 3(h)–3(j)). The detected signals were from the blood stream and the added agent, and as indicated by the imaging details, a higher intensity signal means a larger amount of agent was contained. In the IVI group, the agent was limited to the vessels; the signals were regularly shaped with large high-intensity areas (Figs. 3(e)–3(g)). In the ISI group, areas of high-intensity signals occurred only in the middle of the lumens, which denote primarily the blood stream, but the signals had irregular and larger diameters than the vessel lumens, indicating that the MRI agent was contained in the interstitial space surrounding the vessels (Figs. 3(l)–3(n)). Figures 3(d) and 3(k) show 3D reconstruction images of the entire vascular structure. After IVI, most medium and small vessels were developed and appeared as clear tube-like shapes

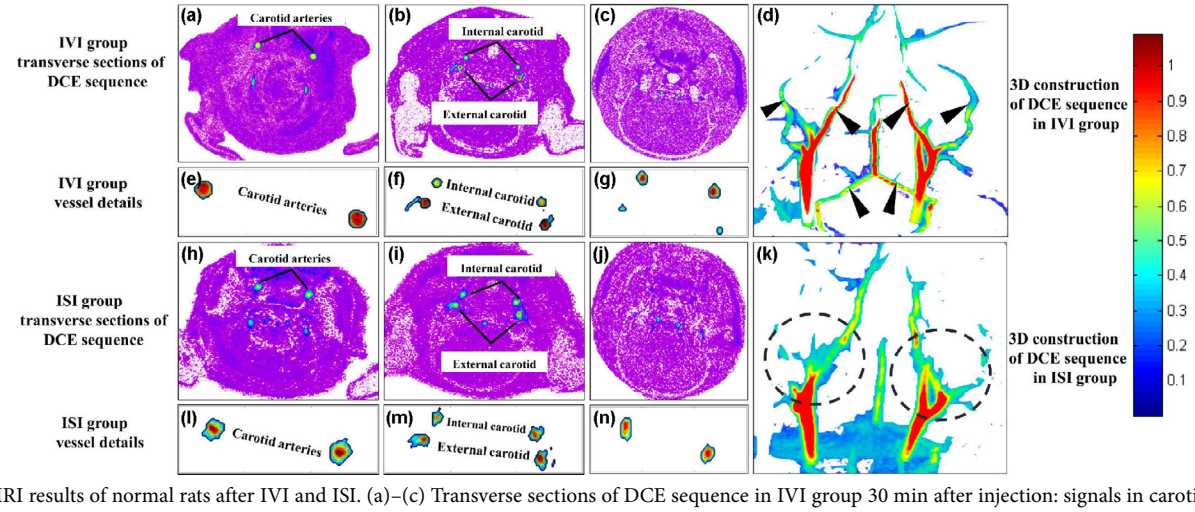

Figure 3 MRI results of normal rats after IVI and ISI. (a)–(c) Transverse sections of DCE sequence in IVI group 30 min after injection: signals in carotid arteries (a), carotid artery branches (b), and intracranial vessels (c) were clear and present in the vessel lumens; (e)–(g) details of (a)–(c). (h)–(j) Transverse sections in the ISI group around the carotid arteries (h), carotid artery branches (i), and intracranial vessels (j), where ambiguous signals were also detected; (l)–(n) details of (h)–(j). (d) and (k) 3D images of DCE sequences 30 min after injection. In the IVI group (d), medium and small vessels were all clearly displayed (arrows), and the carotid arteries and branches showed tube-like signal images. In the ISI group (k), medium and small vessels were not clear, but there were dispersed signals surrounding the carotid arteries and branches (circle).

due to the contained MRI agent (Fig. 3(d)). In contrast, in the ISI group, small vessels were not displayed because little MRI agent was contained in the blood stream. Furthermore, the carotid arteries and branches were not displayed as clearly as those in the IVI group but instead exhibited diffused signals, meaning that the MRI agent was present. All of these results demonstrated that after ISI, the MRI agent in the interstitial architecture formed the interstitial stream just as the blood stream of vessels, and transported upwards through the nonvascular perivascular interstitial space of the carotid arteries.

It has been reported that, at the cortical surface, cerebral arteries extend into pial arteries, and surrounding the pial arteries, pia mater cells comprising a perivascular sheath are present in the subpial space and subarachnoid space. After the pial arteries enter the brain parenchyma, they are called penetrating arterioles and are located in the perivascular space known as the Virchow-Robin space. The fibrous matrix comprising the perivascular space is fully fluid-filled and provides a macroscopic pathway to regulate fluid movement and drainage in the central nervous system (CNS) [11, 21, 22]. We speculated that, in the ISI group, the MRI agent contained in the perivascular interstitial space of the internal carotid arteries was transported through the perivascular sheath of the pial arteries into the Virchow-Robin space and finally reached the brain parenchyma.

3.5 MRI results after BCCAO

When the carotid arteries were ligated, the anterior cerebral circulation was blocked (Figs. S3(a) and S3(b) in the ESM). Because of the flow void effect of the T1-RARE sequence, in the IVI group, there were no differences between the T1-RARE sequences at 0 and 30 min in the vertebral canal (Figs. 4(a) and 4(b)). However, in the ISI group, an increase in MR signal was clearly detected 30 min after injection in the substantia alba medullae spinalis (Figs. 4(f) and 4(g)) compared with the signal at 0 min after injection, which evidenced that the detected signal was not from the blood stream. Furthermore, we compared transverse brain, peripheral brain tissue, and olfactory bulb sections using DCE sequence. In the IVI group, signals occurred in the brain vessels (Figs. 4(c) and 4(d)), and no signal was observed in the olfactory bulb (Fig. 4(e)). In the ISI group, aside from the signals from the brain vessels, there were also signals found in the brain parenchyma (Fig. 4(h)), peripheral brain tissue (Fig. 4(i)), and olfactory bulb (Fig. 4(j)). These differences between the IVI and ISI groups demonstrated that transportation after ISI does not proceed by the same route as that by IVI. From the results, we surmised that, with the blocking of the carotid arteries, the perivascular interstitial space surroundings were also destroyed, and subsequently the interstitial space of the vertebral arteries and peripheral vessels compensated to deliver the agent to the brain. Similarly, Elder et al. reported that intranasally instilled Au ultrafine particles could be deposited in the nose and then travel along the olfactory nerve to the olfactory bulb, where the olfactory neurons provide a pathway for the NPs to enter the CNS [23].

4 Conclusions

In summary, interstitial architecture and its interstitial stream based transportation exist throughout the whole body no matter in physiological or pathological status, which is the pathway not only connecting but also with high efficiency. Additionally, this kind of transportation has its obvious advantages. First and foremost, it is a longitude pathway all over the body and can reach the central nervous system without crossing the BBB. No BBB restriction to limit drugs and NPs delivery to the brain through interstitial stream based transportation, drug accumulation to effective concentrations for the treatment of CNS diseases could be greatly improved. Although intracerebral injection can also deliver drugs to the brain parenchyma, it is an invasive surgery with high risk. Moreover, after IVI, NPs predominantly accumulate in the liver, spleen, and kidney [7], which may cause organ burden or even toxicity. After ISI, drug accumulation in the liver, spleen, and kidney is much lower [14]. Our studies enrich the body of knowledge regarding NP biodistributions and demonstrate the interstitial stream based transportation as a superior route for NP delivery to the brain, which may facilitate the therapeutic effects of drugs and NPs, especially for treating CNS diseases. What we observed with imaging is a macroscopic interstitial architecture-based pathway of perivascular space surrounding the vasculature structure that, with regard to the transportation in viscera and micro-nano scale *in vivo*, cannot be achieved by recent technology. To achieve an ideal transportation route, accurate injection point selection and precise ISI transportation still require further investigation, and advanced equipment is necessary. Furthermore, what we did in this research aimed to use 10 nm nanoparticles as tracers to indicate the exited unique transportation route in the interstitial structure which was different from the blood circulation. We focused on the existence of the route, and next we will further study the affection of the nanoparticles on the transport behaviour.

Acknowledgements

This work was supported by the Chinese Academy of Sciences (No. ZDKYYQ20190002)

Electronic Supplementary Material: Supplementary material (Fig. S1 is schematic diagram of BCCAO and TEM images of brains after BCCAO; Fig. S2 is T1-RARE sequence images of carotid arteries in IVI and ISI groups; Fig. S3 is DCE images after BCCAO

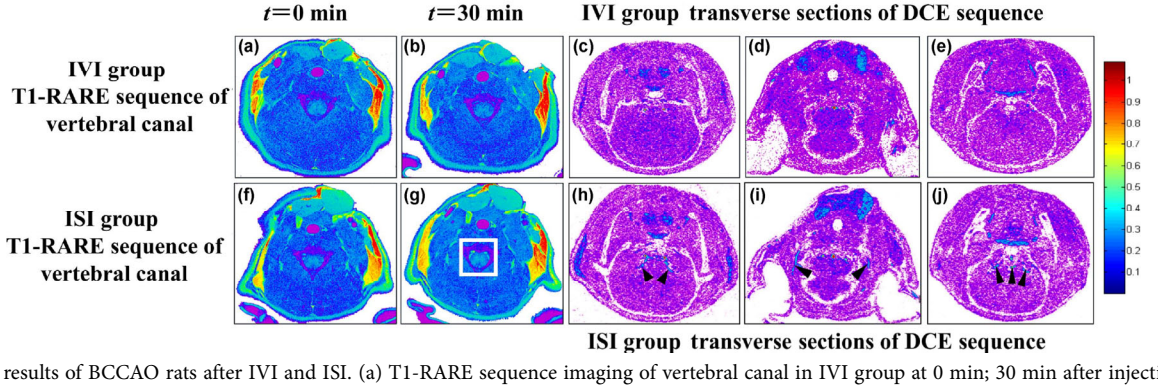

Figure 4 MRI results of BCCAO rats after IVI and ISI. (a) T1-RARE sequence imaging of vertebral canal in IVI group at 0 min; 30 min after injection, no signals were detected in the vertebral canal (b). (c)–(e) Transverse sections of DCE sequence in IVI group 30 min after injection; no signal was detected in the brain parenchyma (c), peripheral brain tissue (d), or olfactory bulb (e). (f) T1-RARE sequence imaging of vertebral canal in ISI group at 0 min. Highlighted signals were present in the substantia alba medullae spinalis 30 min after ISI (white square) (g). (h)–(j) Transverse sections of the ISI group in the brain parenchyma (h), peripheral brain tissue (i), and olfactory bulb (j) showing detected MR signals (black arrows).

in IVI group and ISI group; Movie ESM1 is the movement of the interstitial stream in the interstitial architecture) is available in the online version of this article at https://doi.org/10.1007/s12274-019-2510-9.

References

[1] Dreaden, E. C.; Mackey, M. A.; Huang, X. H.; Kang, B.; El-Sayed, M. A. Beating cancer in multiple ways using nanogold. *Chem. Soc. Rev.* **2011**, *40*, 3391–3404.

[2] Brus, L. Noble metal nanocrystals: Plasmon electron transfer photochemistry and single-molecule Raman spectroscopy. *Acc. Chem. Res.* **2008**, *41*, 1742–1749.

[3] Wijtmans, M.; Rosenthal, S. J.; Zwanenburg, B.; Porter, N. A. Visible light excitation of CdSe nanocrystals triggers the release of coumarin from cinnamate surface ligands. *J. Am. Chem. Soc.* **2006**, *128*, 11720–11726.

[4] Wang, Y. H.; Song, S. Y.; Liu, J. H.; Liu, D. P.; Zhang, H. J. ZnO-functionalized upconverting nanotheranostic agent: Multi-modality imaging-guided chemotherapy with on-demand drug release triggered by pH. *Angew. Chem., Int. Ed.* **2015**, *54*, 536–540.

[5] Khlebtsov, N.; Dyrkman, L. Biodistribution and toxicity of engineered gold nanoparticles: A review of *in vitro* and *in vivo* studies. *Chem. Soc. Rev.* **2011**, *40*, 1647–1671.

[6] Sonavane, G.; Tomoda, K.; Makino, K. Biodistribution of colloidal gold nanoparticles after intravenous administration: Effect of particle size. *Colloids Surf. B Biointerfaces* **2008**, *66*, 274–280.

[7] De Jong, W. H.; Hagens, W. I.; Krystek, P.; Burger, M. C.; Sips, A. J. A. M.; Geertsma, R. E. Particle size-dependent organ distribution of gold nanoparticles after intravenous administration. *Biomaterials* **2008**, *29*, 1912–1919.

[8] Giljohann, D. A.; Seferos, D. S.; Daniel, W. L.; Massich, M. D.; Patel, P. C.; Mirkin, C. A. Gold nanoparticles for biology and medicine. *Angew. Chem., Int. Ed.* **2010**, *49*, 3280–3294.

[9] Iliff, J. J.; Wang, M. H.; Liao, Y. H.; Plogg, B. A.; Peng, W. G.; Gundersen, G. A.; Benveniste, H.; Vates, G. E.; Deane, R., Goldman, S. A. et al. A paravascular pathway facilitates CSF flow through the brain parenchyma and the clearance of interstitial solutes, including amyloid β. *Sci. Transl. Med.* **2012**, *4*, 147ra111.

[10] Morris, A. W. J.; Sharp, M. M.; Albargothy, N. J.; Fernandes, R.; Hawkes, C. A.; Verma, A.; Weller, R. O.; Carare, R. O. Vascular basement membranes as pathways for the passage of fluid into and out of the brain. *Acta Neuropathol.* **2016**, *131*, 725–736.

[11] Jessen, N. A.; Munk, A. S. F.; Lundgaard, I.; Nedergaard, M. The glymphatic system: A beginner's guide. *Neurochem. Res.* **2015**, *40*, 2583–2599.

[12] Venkatesh, B.; Morgan, T. J.; Cohen, J. Interstitium: The next diagnostic and therapeutic platform in critical illness. *Crit. Care Med.* **2010**, *38*, S630–S636.

[13] Swartz, M. A.; Fleury, M. E. Interstitial flow and its effects in soft tissues. *Annu. Rev. Biomed. Eng.* **2007**, *9*, 229–256.

[14] Shi, X. L.; Zhu, Y. T.; Hua, W. D.; Ji, Y. L.; Ha, Q.; Han, X. X.; Liu, Y.; Gao, J. W.; Zhang, Q.; Liu, S. D. et al. An *in vivo* study of the biodistribution of gold nanoparticles after intervaginal space injection in the tarsal tunnel. *Nano Res.* **2016**, *9*, 2097–2109.

[15] Boisselier, E.; Astruc, D. Gold nanoparticles in nanomedicine: Preparations, imaging, diagnostics, therapies and toxicity. *Chem. Soc. Rev.* **2009**, *38*, 1759–1782.

[16] Yang, Y.; Rosenberg, G. A. Blood-brain barrier breakdown in acute and chronic cerebrovascular disease. *Stroke* **2011**, *42*, 3323–3328.

[17] Li, H. Y.; Yang, C. Q.; Lu, K. Y.; Zhang, L. Y.; Yang, J. F.; Wang, F.; Liu, D. G.; Cui, D.; Sun, M. J.; Pang, J. X. et al. A long-distance fluid transport pathway within fibrous connective tissues in patients with ankle edema. *Clin. Hemorheol. Microcirc.* **2016**, *63*, 411–421.

[18] Hu, N.; Cao, Y. P.; Ao, Z.; Han, X. X.; Zhang, Q.; Liu, W. T.; Liu, S. D.; Liao, F. L.; Han, D. Flow behavior of liquid metal in the connected fascial space: Intervaginal space injection in the rat wrist and mice with tumor. *Nano Res.* **2018**, *11*, 2265–2276.

[19] Feng, J. T.; Wang, F.; Han, X. X.; Ao, Z.; Sun, Q. M.; Hua, W. D.; Chen, P. P.; Jing, T. W.; Li, H. Y.; Han, D. A "green pathway" different from simple diffusion in soft matter: Fast molecular transport within micro/nanoscale multiphase porous systems. *Nano Res.* **2014**, *7*, 434–442.

[20] Han, X. X.; Li, H. Y.; Hua, W. D.; Dai, L. R.; Ao, Z.; Liao, F. L.; Han, D. Fluid in the tissue channels of vascular adventitia investigated by AFM and TEM. *Clin. Hemorheol. Microcirc.* **2017**, *67*, 173–182.

[21] Kulik, T.; Kusano, Y.; Aronhime, S.; Sandler, A. L.; Winn, H. R. Regulation of cerebral vasculature in normal and ischemic brain. *Neuropharmacology* **2008**, *55*, 281–288.

[22] Zhang, E. T.; Inman, C. B.; Weller, R. O. Interrelationships of the pia mater and the perivascular (Virchow-Robin) spaces in the human cerebrum. *J. Anat.* **1990**, *170*, 111–123.

[23] Elder, A.; Gelein, R.; Silva, V.; Feikert, T.; Opanashuk, L.; Carter, J.; Potter, R.; Maynard, A.; Ito, Y.; Finkelstein, J. et al. Translocation of inhaled ultrafine manganese oxide particles to the central nervous system. *Environ. Health Perspect.* **2006**, *114*, 1172–1178.